71st International Astronautical Congress (IAC) – The CyberSpace Edition, 12-14 October 2020.

IAC-20-A3.2B.8.x58028

Predicting the Outcome of the LUMIO Lunar CubeSat

Gianmario Merisio[1], Mauro Massari[2], Pierluigi Di Lizia[3], James Douglas Biggs[4], Carmine Giordano[5], Vittorio Franzese[6], Francesco Topputo[7], Detlef Koschny[8], Johan Vennekens[9], Roger Walker[10]

The Lunar Meteoroid Impacts Observer (LUMIO) is a CubeSat mission to observe, quantify, and characterise the meteoroid impacts by detecting their flashes on the lunar far-side. This complements the knowledge gathered by Earth-based observations of the lunar nearside, thus synthesising a global information on the lunar meteoroid environment. In this work, we present the methodology developed to predict LUMIO's scientific contribution to refine the current meteoroid flux models in the solar system. Our approach relies on a combined modelling and simulation of LUMIO's Payload, Orbit, and Environment (POE). The LUMIO-POE tool has been developed in order to conduct preliminary parametric analyses, which feed back the design of both the payload and the mission operative orbit. Our results indicate that the present-day LUMIO mission has the potential to detect up to 31 impacts per day due to sporadic events in the range of impact kinetic energy at Earth $[10^{-6}, 10^{-1}]$ kton TNT. Considering the same kinetic energy range, LUMIO has the potential to detect up to 133 impacts per day belonging to meteoroid showers during the peak of the Geminids. That neglecting stray light noise. Peaks of daily data rate greater than 1000 Mbit/deg are reached during the activity period of the Geminids. At the end of the operative phase, more than 25 Gbit of scientific data are expected to be produced.

1 Introduction

The Earth–Moon system is constantly bombarded by meteoroids of different sizes, and their numbers are significant. Fragments of asteroids and comets, that date back to planetary formation times, constantly encounter the Earth and Moon in their orbits, and impact them as meteoroids. Observations of meteor showers on Earth have been studied for at least 50 years [1], in order to construct Solar System meteoroid models. These models can be useful in, e. g., predicting the small-meteoroid flux that deteriorates space equipment or when the next large meteoroid will impact the Earth itself. As meteoroids originate from asteroids and comets, meteoroid models can also be used to understand the spatial distribution of those objects near the Earth–Moon system.

By observing the lunar surface impacts, whose flux is similar to that of the Earth, we could obtain detailed information regarding their magnitudes, velocities, temporal and spatial distributions. These information can be used to increase confidence of meteoroid models, to validate the existing lunar impact models, to contribute to lunar seismology studies and interior modelling, and to initiate a Lunar Situational Awareness programme for future exploration missions.

Earth-based optical observations of the light flashes produced by lunar meteoroid impacts have revealed useful in the validation and improvement of meteoroid models [2]. Monitoring the Moon for meteoroid impact flashes allows for the observation of larger areas than those covered by traditional surveys of Earth's upper atmosphere. Thus, theoretically, more meteoroid impacts can be detected in shorter periods of time [3]. Moreover, Earth-based lunar observations are restricted by weather, geometric, and illumination conditions. As such, a lunar CubeSat can improve the detection rate

---

[1] PhD Candidate, Department of Aerospace Science and Technology, Politecnico di Milano, Via La Masa 34, 20156, Milano, Italy, gianmario.merisio@polimi.it

[2] Associate Professor, Department of Aerospace Science and Technology, Politecnico di Milano, Via La Masa 34, 20156, Milano, Italy, mauro.massari@polimi.it

[3] Assistant Professor, Department of Aerospace Science and Technology, Politecnico di Milano, Via La Masa 34, 20156, Milano, Italy, pierluigi.dilizia@polimi.it

[4] Associate Professor, Department of Aerospace Science and Technology, Politecnico di Milano, Via La Masa 34, 20156, Milano, Italy, jamesdouglas.biggs@polimi.it

[5] PhD Candidate, Department of Aerospace Science and Technology, Politecnico di Milano, Via La Masa 34, 20156, Milano, Italy, carmine.giordano@polimi.it

[6] PhD Candidate, Department of Aerospace Science and Technology, Politecnico di Milano, Via La Masa 34, 20156, Milano, Italy, vittorio.franzese@polimi.it

[7] Associate Professor, Department of Aerospace Science and Technology, Politecnico di Milano, Via La Masa 34, 20156, Milano, Italy; francesco.topputo@polimi.it

[8] Planetary Scientist, European Space Research & Technology Centre (ESTEC), ESA, Postbus 299, 2200 AG, Noordwijk, The Netherlands; detlef.koschny@esa.int

[9] Systems Engineer, European Space Research & Technology Centre (ESTEC), ESA, Postbus 299, 2200 AG, Noordwijk, The Netherlands; johan.vennekens@esa.int

[10] Head of CubeSat Systems Unit, European Space Research & Technology Centre (ESTEC), ESA, Postbus 299, 2200 AG, Noordwijk, The Netherlands; roger.walker@esa.int

of lunar meteoroid impact flashes, as it would allow for longer monitoring periods. Moreover, it being closer to the Moon surface, a lunar CubeSat could also allow for the detection of meteoroids smaller than millimetres [4].

LUMIO is a CubeSat mission to a halo orbit at Earth–Moon L_2 that shall observe, quantify, and characterise meteoroid impacts on the Lunar farside by detecting their flashes, complementing Earth-based observations on the Lunar nearside, to provide global information on the Lunar Meteoroid Environment and contribute to Lunar Situational Awareness. LUMIO was awarded ex-aequo winner of the European Space Agency's challenge Lunar CubeSat for Exploration, under the SysNova framework, and as such it is being considered for implementation in the near future. The Phase A design has been conducted in 2020 under ESA GSTP contract, after a successful, independent mission assessment performed by ESA's CDF team. The consortium of the Phase A design is formed by Politecnico di Milano, Leonardo S.p.a., ISISPACE, Delft University of Technology, and S[&]T Norway. LUMIO mission is conceived to address the following issues:

- **Science Question**. What are the spatial and temporal characteristics of meteoroids impacting the lunar surface?
- **Science Goal**. Advance the understanding of how meteoroids evolve in the cislunar space by observing the flashes produced by their impacts with the lunar surface.
- **Science Objective**. Characterise the flux of meteoroids impacting the lunar surface.

The mission utilises a 12U form-factor CubeSat which carries the LUMIO-Cam, an optical instrument capable of detecting light flashes in the visible spectrum to continuously monitor and process the data. The mission implements a novel orbit design and latest CubeSat technologies to serve as a pioneer in demonstrating how CubeSats can become a viable tool for deep space science and exploration. The selected operative Earth–Moon L_2 quasi-halo orbit of LUMIO expressed in the Earth–Moon synodic frame is shown in Fig. 1. The ranges of LUMIO from the Moon and the Earth are plotted in Fig. 2 to provide a better understanding of the mission.

In this work, the methodology developed to predict LUMIO's scientific contribution to refine the current meteoroid flux models in the solar system is presented. Combining the modelling and simulation of LUMIO's payload, orbit, and environment allow to conduct preliminary parametric analyses. LUMIO-POE is the tool in charge of performing such analyses. LUMIO-POE has an inner engine and several modules. Worth to mention is the *Meteoroid Gun* (MeGun) toolkit, which models numerous known meteoroid showers as well as sporadic impacts with the lunar surface.

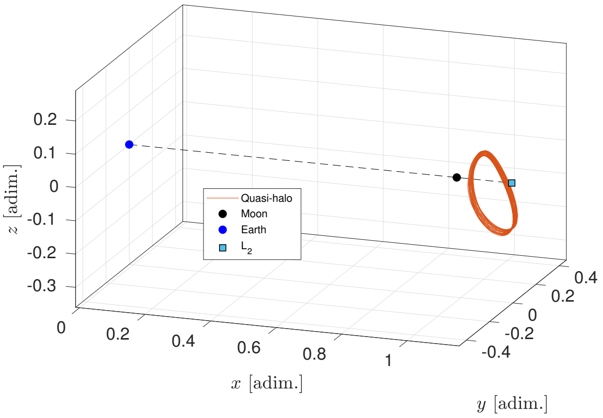

Fig. 1: Selected operative Earth–Moon L_2 quasi-halo orbit in the Earth–Moon synodic frame.

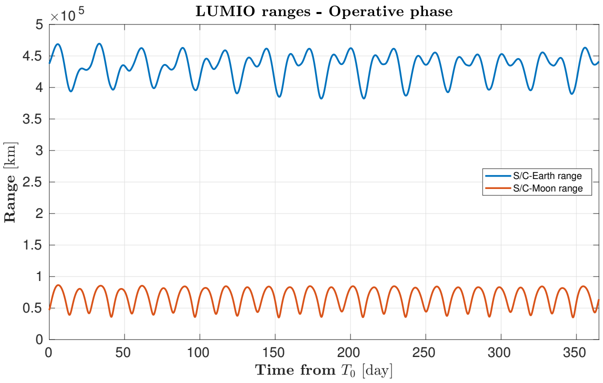

Fig. 2: Ranges of LUMIO from the Moon and the Earth during the operative phase.

The remainder of the paper is organized as follows. In Section 2 the modelling of the meteoroid environment is introduced. The description of the payload modelling is provided in Section 3. In Section 4, the results obtained running the simulation of the meteoroid environment are presented. Results about the radiometric analysis and the estimated payload data return follows in Section 5, and Section 6, respectively. Concluding remarks are given in Section 7.

2 Modelling of the meteoroid environment

The Earth–Moon system encounters meteoroids continuously while orbiting around the Sun. The meteoroid environments of the Earth and the Moon are similar but not identical. Indeed, the Moon and the Earth are placed in distinct locations of the space. Furthermore, they exert different gravitational attractions. As a consequence, the following phenomena should be taken into account in the modelling of the meteoroid environment: the distance from the meteoric filament, the gravitational acceleration, and the gravitational focusing.

Distance from the meteoric filament. Meteoroids are distributed with variable density across the meteoric filament. It is assumed that the meteoric filament can be approximated as a tube where the meteoroid density decreases linearly from the central axis of the tube itself [5]. The values of the meteoroid density of the Earth and the Moon depend on their positions with respect to the meteoric filament central axis. However, the Earth–Moon distance is negligible with respect to the extent of a filament [6]. Consequently, it is reasonable to assume that the meteoroid density perceived by the Moon and the Earth is the same [5].

Gravitational acceleration. When entering the SOI of a celestial body, a meteoroid is subjected to its gravitational force. The geocentric velocity is increased according to

$$V_{imp} = \sqrt{V^2 + 2\frac{\mu}{R}} \tag{1}$$

where V is the geocentric velocity of the meteoroid, μ is the gravitational mass parameter of the attractor, and R is the radius of the attractor [2].

Gravitational focusing. When a meteoroid enters the SOI of a celestial body, its trajectory is bent by the gravitational force of the attractor. That causes an increase of the number of impacts. Due to the gravitational focusing, the celestial body has an effective cross sectional area larger than the physical one. Therefore, a fictitious radius of the attractor R^* larger than the real one is introduced. The fictitious radius is given by

$$R^* = R\sqrt{1 + 2\frac{\mu}{V^2 R}} \tag{2}$$

and as a result the effective target area of the attractor is increased [2].

Knowledge about the meteoroid environment comes from astronomical observations. Experimental data are collected and validated. From those data, descriptive parameters of meteoroid showers and sporadic background are derived [7, 8].

2.1 Meteoroid showers

The International Astronomical Union is the entity in charge of tracking reported meteoroid showers. Currently, there are 932 reported meteoroid showers in the International Astronomical Union Meteor Data Center database[1]. Among them, 112 are established meteoroid showers [9].

The following parameters are used to describe a shower. The zenith hourly rate ZHR characterises the strength of the flux [10]. The mass distribution index s tells how meteoroid masses are distributed within a shower. The mass distribution index is computed through the relation

$$s = 1 + 2.5\log_{10}(\chi) \tag{3}$$

where χ is the population index. The population index of a shower is derived experimentally [11].

Showers depend strongly on the time epoch. They show activity periods that repeat annually. The ZHR varies in time. It rises between the start and the peak of the activity period. Then, it decreases from the peak to the shower end. The time dependence is expressed in terms of solar longitude $\lambda_\odot$. The equation used to describe the ZHR variation is

$$\mathrm{ZHR} = \mathrm{ZHR}^{max}\frac{(W/2)^2}{\left(\left(\lambda_\odot - \lambda_\odot^{max}\right)^2 + (W/2)^2\right)} \tag{4}$$

where $\lambda_\odot$ and W are expressed in degrees. W is the full-width-half-maximum. ZHR^{max} is the peak rate at the peak solar longitude $\lambda_\odot^{max}$ [12]. Additionally, Meteoroid showers experience yearly variations in the flux and in the epoch of the activity peak. Rare events like outbursts could also occur. Yearly variations and outbursts are not taken into account in this work.

Any shower has its peculiar geocentric velocity and radiant direction. The radiant direction is expressed in terms of right ascension RA and declination DEC. Since the activity period of a shower lasts for some days, the radiant drifts in time due to the Earth's motion about the Sun. This behaviour is characterised in terms of right ascension drift ΔRA and declination drift ΔDEC of the radiant itself.

The last parameter is the bulk density ρ of a meteoroid. That is retrieved from meteorites and from photographic observation techniques [13]. The density ranges from 1600 to $7370\,\mathrm{kg\,m^{-3}}$. The porosity and the chemical composition of the impactor affect the density value. The lower value is associated to carbonaceous meteorites. On the other hand, the higher value is associated to iron meteorites [14].

2.2 Sporadic background

The model chosen for this study takes into account 7 different sources for the sporadic background which con-

---

[1] The Meteor Data Center database is available at `http://pallas.astro.amu.edu.pl/~jopek/MDC2007/index.php` (visited on 29/09/2020).

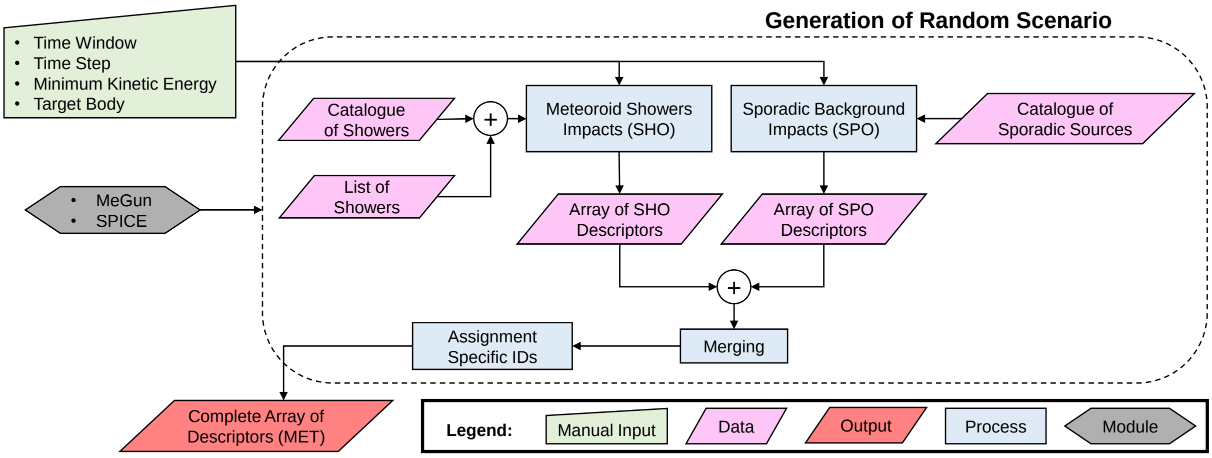

Fig. 3: Schematic representation of a random scenario generation.

stitute the radiant-resolved model [15]. They are: the isotropic source, the helion source, the anti helion source, the north apex source, the south apex source, the north toroidal source, and the south toroidal source.

The flux of the sporadic background is described with the hourly rate HR. In literature, the common practice is to assume HR $= 10\,\text{h}^{-1}$ [5, 16–18]. The hourly rate is an indication of the total flux of the sporadic background. The sources have different strengths, which are provided by the radiant-resolved model [15]. The isotropic source shows the biggest flux, accounting for the 42% of the total number of impacts. The other sources have smaller strengths. Also the sources of the sporadic background are parametrized with mass distribution and population indexes [19].

Information about geocentric velocity and radiant direction of each source are provided in [15]. The radiant direction is not defined for the isotropic source since, by definition, it is equally distributed in space.

2.3 Numerical simulation of the meteoroid environment

MeGun is in charge of the numerical simulation. MeGun is one of the modules of the wider LUMIO-POE methodology. MeGun generates the meteoroid environment randomly, with a statistical approach, breeding each meteoroid singularly. Essentially, it is a gun that shoots meteoroids to a target. The target may be the Moon or the Earth. In this work, the target is the Moon.

The basis of MeGun resides in the experimental observations of fireballs, impact flashes, and meteors. The approach is statistical because observations are affected by uncertainties on measurements and forecasting. Indeed, meteoroid streams are dynamic entities, which are subjected to yearly variation in the flux and in the maximum peak activity [6].

2.4 Overview of meteoroid impact generation

MeGun takes as input: the desired target, the time span to be simulated, the time step, and the minimum impact kinetic energy of the meteoroids to breed. It returns a set of descriptors for each impact. The generation of meteoroids belonging to showers is independent to that of meteoroids coming from the sporadic background. MeGun relies on SPICE routines [20, 21].

The minimum threshold of impact kinetic energy is needed because meteoroid flux models are not limited for decreasing kinetic energy. Thus, the number of meteoroids tends to infinity when the kinetic energy approaches zero. Furthermore, for some applications, it is known a threshold on the minimum kinetic energy. In this way only useful impactors are generated, decreasing the computational burden.

MeGun has a meteoroid showers and sporadic background catalogue embedded [22]. The catalogue was built collecting and merging information from the International Astronomical Union Meteor Data Center database and from catalogues found in literature [10, 12, 13, 19, 23–26].

The generation procedure of meteoroids belonging to meteoroid showers is the following [22]:

i) the time window is discretised and an array of time epochs is built;

ii) for each time interval, it is checked which showers are active;

iii) for the active showers, the number of meteoroids to produce is computed;

Tab. 1: LUMIO-Cam specifics.

Specific	**Symbol**	**Value**
CCD detector	ID	e2v CCD201-20
Focal length	FL	127 mm
F number	$F_\#$	2.5
Aperture diameter	D	50.80 mm
Field of view	FOV	6 deg
Sensitivity range	$[\lambda_1, \lambda_2]$	$[450, 950]$nm
Dichroic wavelength	λ_{dic}	820 nm
Active pixels	N_{pix}	1 Mpixel
Pixel size	d_{pix}	13.3 µm
Exposure time	Δt_{exp}	66 ms
Frame per second	FPS	15 fps
Low noise gain	G	$[1, 1000]$
Excess noise factor	F	$\sqrt{2}$
Polychromatic ensquared energy in 1 pixel	f_{ensq}	0.89
Dichroic transmissivity	η_{dic}	0.9

iv) the meteoroids are generated and the set of descriptors is returned.

The generation procedure of meteoroids coming from the sporadic background is the following [22]:

i) given the minimum impact kinetic energy and the width of the time window, the number of sporadic meteoroids is determined;

ii) the meteoroids are generated and the set of descriptors is returned.

The schematic representation of a random scenario generation is shown in Fig. 3.

3 Modelling of the LUMIO-Cam

The peculiarity of the LUMIO-Cam is the presence of two channels, the Visible Spectrum channel (VIS) and the Near-Infrared wavelength Range channel (NIR). The incoming light is split at 820 nm by means of a dichroic. Each channel is equipped with the same CCD detector. The LUMIO-Cam takes pictures with exposure time $\Delta t_{exp} = 66\,\mathrm{ms}$, meaning that the P/L works at 15 fps. The list of LUMIO-Cam specifics is presented in Tab. 1. Currently, an entrance baffle grants that no direct sunlight hits first lens at sun angles larger than 17.5 deg [27].

The SNR is defined in [28] as

$$\mathrm{SNR} = \frac{s_i}{\sigma} \tag{5}$$

where s_i is the signal, in e^-, of a generic source of interest while σ is the Poisson noise, in e^- *rms* (Root-Mean-Square), associated with all signals collected by the detector. The signal s_i and σ refer to the single pixel. The Poisson noise of a source i is given by [28]

$$\sigma_i = \sqrt{s_i} \tag{6}$$

while the total Poisson noise is obtained as follows [28]

$$\sigma = \sqrt{\sum_i \sigma_i^2} = \sqrt{\sum_i s_i} \tag{7}$$

In the specific case of the LUMIO-Cam, the Signal-to-Noise Ratio (SNR) of an impact flash must be computed for both VIS and NIR.

3.1 Impact flash duration in LUMIO-Cam frames

It is assumed that the channels are perfectly synchronized, therefore, they take pictures of the Moon simultaneously. Generally speaking, a flash may occur at any time, which means that the starting times of the impact flash and the photographic frame may not coincide. This fact and other phenomena are taken into account when computing the SNR. Therefore, the flash duration in simultaneous frames of the two channels is exactly the same. This assumption is not true in the real world, but it is assumed that the synchronization errors are negligible with respect to the integration time of a frame.

3.2 Signal peak location

In this study, it is assumed that the impact occurs close to the sub-satellite point and that the signal peak is contained in the central pixel of the LUMIO-Cam CCD detector. Specifically, 3 significant cases are identified:

1. the peak location is exactly at the centre of the pixel and the impact flash is completely contained within 1 pixel (spread fraction equal to 1);
2. half of the point spread function of the impact flash is contained within the pixel, which is expected to be the most common case (spread fraction equal to 1/2);
3. the peak location coincides with one of the 4 corners of the pixel (spread fraction is equal to 1/4).

3.3 Impact flash signal

The procedure to compute the signal coming from the impact flash is based on the fact that the impact raises a plume made of ejecta material. Such plume emits radiation which can be detected. An equivalent black body temperature is associated to the radiating plume. Generally speaking, the radiating plume cools down after

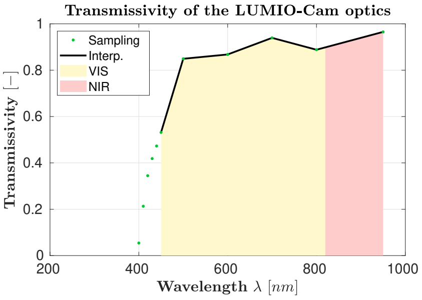

Fig. 4: Transmissivity of the LUMIO-Cam optics, dichroic contribution not included. The bandwidths received by VIS and NIR channels are highlighted with different colours. Sampling points are represented by point markers. The curve is a piecewise linear interpolation performed with MATLAB®. Courtesy of Leonardo S.p.a..

the impact, hence, the equivalent black body temperature decreases in time [29]. The cooling process is not modelled in MeGun. Nevertheless, MeGun computes an equivalent black body temperature assumed constant in time.

To compute the signal, it has been taken into account: the sensitive spectrum range of the LUMIO-Cam, the dichroic wavelength, the aperture diameter, the fraction of polychromatic ensquared energy in 1 pixel, the attenuation effects of the optics (bulk absorption, real coating transmission, dichroic lens transmission), the Quantum Efficiency (QE) of the equipped CCD detector, the gain of the LUMIO-Cam, the distance from the impact location, and the impact dynamics (equivalent black body temperature of the plume, plume area, and flash duration).

Attenuation effects of the optics. The presence of optics causes some attenuation effects acting on the signal. The transmissivity defines the number of photons which do not get reflected by the optics. The curve describing the transmissivity of the optics at the wavelengths corresponding to the sensitive spectrum range of the camera is shown in Fig. 4. The curve takes into account how the bulk absorption and the real coating affect the transmissivity $\xi(\lambda)$ of the LUMIO-Cam. Regarding how the dichroic lens affects the performance of the LUMIO-Cam, it is assumed that the dichroic transmissivity is equal to $\eta_{\mathrm{dic}} = 0.9$.

Quantum Efficiency of the CCD detector. The QE is used to convert the photons number at a given wavelength into a number of electrons. The QE curve of the selected detector is shown in Fig. 5.

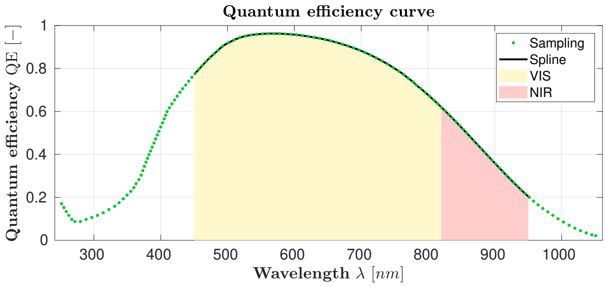

Fig. 5: QE curve of CCD201-20 detector. The bandwidths received by VIS and NIR channels are highlighted with different colours. Sampling points are represented by point markers. The curve is a spline interpolation performed with MATLAB®.

Distance from the impact location. For the radiometric analysis, the minimum, the average, and the maximum distances of the LUMIO CubeSat from the centre of the Moon during the operative phase of the mission have been used as study cases. Specifically, they are: $r_{\mathrm{min}} = 35\,878\,\mathrm{km}$, $r_{\mathrm{mean}} = 61\,048\,\mathrm{km}$, and $r_{\mathrm{max}} = 86\,218\,\mathrm{km}$. The distance from the impact location is computed subtracting the radius of the Moon to the LUMIO–Moon distance.

Impact dynamics. To perform the radiometric analysis, the impact dynamics quantities needed to compute the SNR are retrieved simulating the meteoroid environment with MeGun.

3.4 Computation of the flash signal

The formula of the impact flash signal s_{imp} is

$$
\begin{aligned}
s_{\mathrm{imp}} &= \frac{A_{\mathrm{oa},\perp}}{A_d} A_p \tau_i \int_{\lambda_1}^{\lambda_2} N_{e^-}(\lambda, T_{\mathrm{imp}}) \mathrm{d}\lambda \\
&= \frac{D^2 \cos(\theta)}{4\ f d_{\mathrm{imp}}^2} A_p \tau_i \int_{\lambda_1}^{\lambda_2} N_{e^-}(\lambda, T_{\mathrm{imp}}) \mathrm{d}\lambda
\end{aligned}
\tag{8}
$$

where $A_{\mathrm{oa},\perp} = \pi D^2 \cos(\theta)/4$ is the surface of optics aperture perpendicular to the vector pointing towards the impact location. $A_d = f \pi d_{\mathrm{imp}}^2$ is the area used to scale the signal at observer distance. D is the aperture diameter. θ is the angle between the boresight direction and the vector pointing towards the impact location, which is zero, since it is assumed that the impact happens at the sub-satellite point. f is the anisotropy degree used in MeGun. τ_i is the flash duration in the frame considered. A_p is the radiating plume area. $[\lambda_1, \lambda_2]$ is the domain in which the function $N_{e^-}(\lambda, T)$ is integrated. Note that, due to the presence of the dichroic, the integration domains for VIS and NIR are different.

Tab. 2: MeGun setups.

Setup		Value
Target	-	Moon
Time window start	t_i	1 January 2024 12:00:00.0 UTC
Time window End	t_f	1 January 2025 12:00:00.0 UTC
Time step	Δt	1 h
Minimum kinetic energy at the Moon	$\mathrm{KE}_{☾,\mathrm{min}}$	7.1×10^{-7} kton TNT
Minimum kinetic energy at the Earth	$\mathrm{KE}_{\oplus,\mathrm{min}}$	1×10^{-6} kton TNT
Maximum kinetic energy at the Moon	$\mathrm{KE}_{☾,\mathrm{max}}$	7.1×10^{-2} kton TNT
Maximum kinetic energy at the Earth	$\mathrm{KE}_{\oplus,\mathrm{max}}$	1×10^{-1} kton TNT
Random scenarios	N_{scn}	10^3

3.5 Noise sources

The noise sources taken into account in the SNR computation are:

- the noise associated with the impact signal itself σ_{imp} (or photon shot noise);
- the moon surface background noise $\sigma_{☾}$;
- the dark current (or internal noise of CCD) σ_{DC};
- the readout noise of CCD σ_{RON};
- the off-chip noise of CCD σ_{OCN};
- the quantization noise generated by the analogue to digital converter σ_{QN}.

In this preliminary analysis the stray light noise has been neglected.

3.6 SNR computation

The detectors mounted in the two channels allow to amplify the signals generated in the pixels, before the multiplication register, by a factor G. Such signals are: s_{imp}, $s_{☾}$, and s_{DC}. The gain G may be varied from 1× to 1000×. The signal amplification increases also the total Poisson noise. That is accounted by means of the excess noise factor F. The expression to evaluate the SNR is

$$\mathrm{SNR} = 10 \log_{10} \left(G s_{\mathrm{imp}} \left(F^2 \, G \left(\sigma_{\mathrm{imp}}^2 + \sigma_{☾}^2 + \right. \right. \right. \\ \left. \left. \left. + \sigma_{\mathrm{DC}}^2 \right) + \sigma_{\mathrm{RON}}^2 + \sigma_{\mathrm{OCN}}^2 + \sigma_{\mathrm{QN}}^2 \right)^{-\frac{1}{2}} \right) \tag{9}$$

where the results is in dB. Note that if the signal is not amplified ($G = 1$) the excess noise factor should not be included in the formula. The numerical value taken from the detector's datasheet and used for the excess noise factor is $F = \sqrt{2}$.

4 Meteoroid environment simulations results

The results of the simulations run with MeGun are herewith presented. The setups used are collected in Tab. 2.

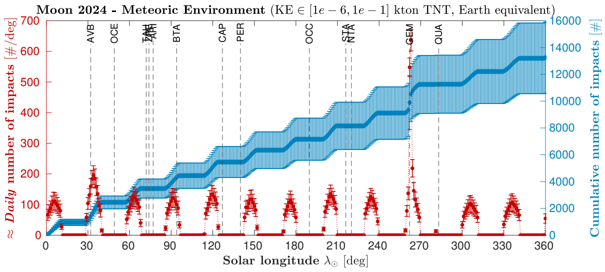

Fig. 6: Temporal distribution of the scientific output – year 2024. On the left y-axis, in red, estimated daily detections as a function of solar longitude. On the right y-axis, in blue, cumulative number of impacts as a function of solar longitude. Results shown in 1 deg bins of solar longitude. The vertical dashed black lines mark activity period peaks of major showers. Stray light noise neglected. Statistical results obtained from 1000 runs.

Each random scenario is propagated for 1 year. In these simulations the focus is on the impacts with kinetic energies within the range of interest for the mission.

4.1 Scientific output estimation

The plot in Fig. 6 shows the temporal distribution in 1 deg bins of solar longitude of the estimated scientific output of the mission. To perform an estimation, since not all the meteoroids generated by MeGun can be observed by LUMIO, only the potentially detected impacts are retained. The events not retained are those that: *i*) impact the Moon in the illuminated side; *ii*) impact the Moon in the nearside; *iii*) impact the Moon when the illumination of the farside is greater than 50% [30]; *iv*) are out of the impact kinetic energy range $[10^{-6}, 10^{-1}]$ kton TNT at the Earth; *v*) whose visibility is obstructed by natural features (e.g., mountains) of the Moon (50% chance that this occurs). The red peak in Fig. 6, which is due to the Geminids shower, has been used to infer the highest expected daily rate of impacts ascribable to meteoroid showers.

Tab. 3: Statistics about impact dynamics.

Quantity	**Value**
$\mathcal{N}_{\text{pool}}$	389 722
Black body temperature	
μ_T	2100 K
σ_T	170 K
$\pm 3\sigma_T$ Range	[1590, 2610]K
$T_{\min}$	1100 K
$T_{\max}$	2800 K
Flash duration	
μ_τ	13 ms
σ_τ	18 ms
$\pm 3\sigma_\tau$ Range	(0, 67]ms
$\tau_{\min}$	8×10^{-4} ms
$\tau_{\max}$	1.8 ms
Plume area	
μ_{Ap}	47 m^2
σ_{Ap}	100 m^2
$\pm 3\sigma_{Ap}$ Range	(0, 347]m^2
$A_{p,\min}$	4 m^2
$A_{p,\max}$	21 360 m^2

4.2 Synthesis of impact dynamics

A single sample scenario of year 2024 has been selected to conduct a synthesis about the impact dynamics. Considering that single sample scenario, the meteoroids with impact kinetic energy within the range $[10^{-6}, 10^{-1}]$ kton TNT at the Earth (corresponding to $[7.1 \times 10^{-6}, 7.1 \times 10^{-2}]$ kton TNT at the Moon) are 389 722. This is a pool of sample large enough to obtain meaningful statistical results. The results in terms of means and standard deviations of equivalent black body temperature of the flash, impact flash duration, and size of the plume areas have been computed and are shown in Tab. 3. A comment about the results follows.

Considering the $\pm 3\sigma_T$ range, the equivalent black body temperatures are included between 1590 K and 2610 K. This range is entirely limited between the minimum and maximum temperature measured within the NELIOTA project and reported in [14] ($T_{\text{min,NELIOTA}} =$ 1600 K, $T_{\text{max,NELIOTA}} = 3100$ K). In [31], it is suggested a reasonable temperature range of $[1700, 3800]$ K which is coherent with the derived results, although the maximum temperature returned by MeGun is lower. The obtained mean is slightly lower than the reference value proposed by [32], but it must be taken into account that MeGun does not compute the peak temperature.

According to [29], impact flash duration ranges from ≈ 10 ms to ≈ 1 s. The NELIOTA programme reports durations between 33 ms and 165 ms, where the lower bound is the exposure time of its cameras. Similarly, flashes that last from 20 ms to 160 ms are reported in [5]. During the mission Phase-*0* design it was assumed a duration of 30 ms [33, 26]. Differently, [34, 35] used 10 ms for the orbital trade-off. Considering the truncated $\pm 3\sigma_\tau$ range (flash durations are positive) values from 0 ms and up to 67 ms are found. The results have the same order of magnitude of the ones reported in literature. Nevertheless, the average duration is slightly smaller than the typical values employed or reported in literature.

Tab. 4: LUMIO-Cam internal Poisson noises.

Source	**Poisson Noise** [e$^-$ rms]
σ_{DC}	3.31
σ_{RON}	7.06
σ_{OCN}	1.01×10^2
σ_{QN}	9.00

Tab. 5: Poisson noise of the Moon's background

	Channel:	**VIS**	**NIR**
$\sigma_{\leftmoon}$ *	[e$^-$ rms]	7.60×10^{-18}	1.21×10^{-14}

* Computations performed in the planar approximation and with impact occurring at nadir.

Considering the truncated $\pm 3\sigma_{Ap}$ range, the plume areas span from 0 m^2 up to 347 m^2. Like for the impact flash durations, the $\pm 3\sigma_{Ap}$ range has been truncated to return only positives values.

5 Radiometric analysis results

To be conservative, the radiometric analysis has been performed setting the minimum SNR to 10 dB. Since the results have been obtained relying on the statistical approach of MeGun, the condition of saturation is not clearly demarcated. Therefore, the saturation condition has been set to occur when more than half of the impacts at specific conditions saturate the detector. Note that the stray light noise has been neglected in this preliminary analysis.

First of all, Poisson noises affecting the impact flash detections are computed. Dark current noise, read out noise, off-chip noise, and quantization noise depend only on the LUMIO-Cam specifics and are the same for both channels. Their values are collected in Tab. 4. On the contrary, the Moon's surface background noise depends on the channel, see Tab. 5. Remember that the Moon's surface background noise is computed assuming that the impact occurs at nadir and in the planar approximation, therefore it is independent from the impact distance.

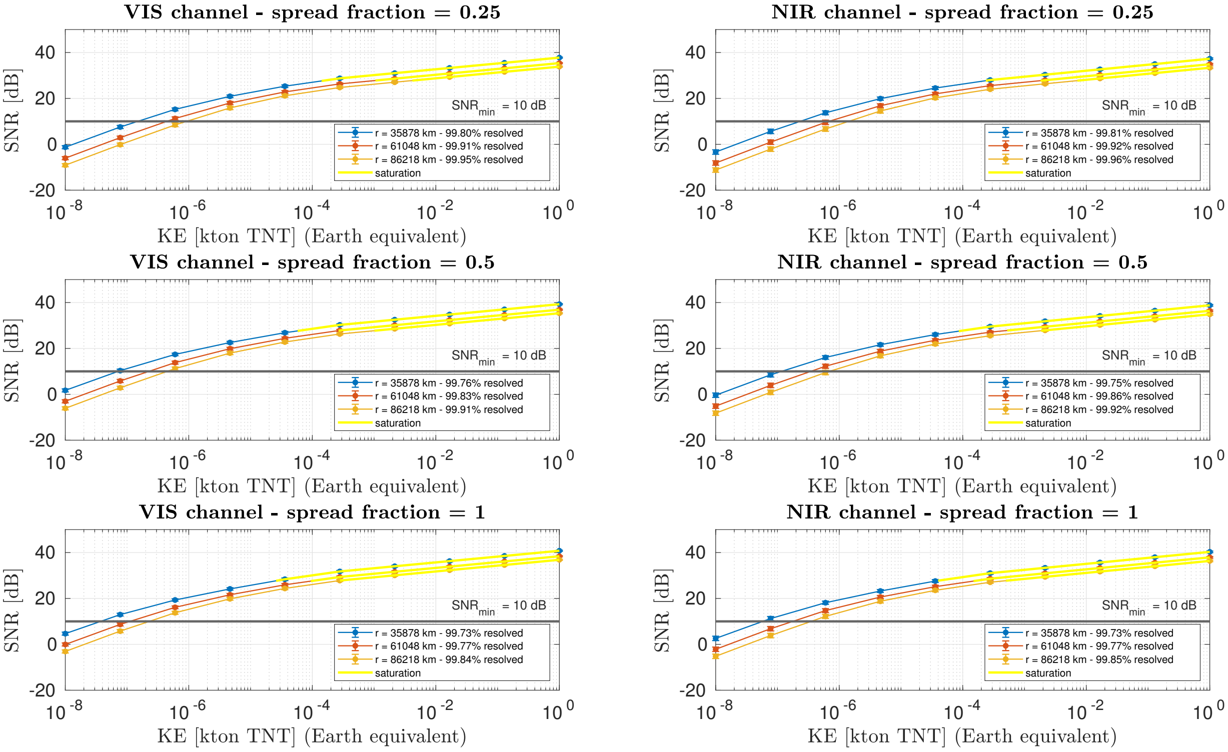

Fig. 7: Radiometric analysis. SNR as a function of impact kinetic energy in Earth equivalent. SNR trends in the two channels for 3 different cases of spread fraction. In each plot, the SNR for different LUMIO–Moon distances is plotted. In yellow, impact kinetic energies that saturate the detectors. The black horizontal line marks the threshold of minimum SNR. Legends contain the percentage of resolved impacts. Gain fixed to 10. For each given impact kinetic energy, 1000 impacts have been simulated. Stray light noise neglected. Semi-log scale plots.

The firs set of results is about how the SNR varies with respect to the the impact kinetic energy of the meteoroid expressed in Earth equivalents. Results are shown in Fig. 7. The charts present the different behaviour of the two channels at different distances of LUMIO from the Moon and for the 3 significant cases of signal peak location. The impact energies that saturate the detector are highlighted in yellow. The charts have been plotted fixing the gain of the LUMIO-Cam at 10. For each given impact kinetic energy, 1000 impacts have been simulated to obtain the average SNR.

Clearly the range of impact kinetic energies which can be detected depend strongly on the distance from the Moon and on the spread fraction of the impact flash on the pixel. Note that the most common case should be the one in which the spread fraction is 1/2. From the chart, it is clear that keeping the gain fixed does not allow to cover properly the whole range of impact kinetic energies in which the mission is interested (range of kinetic energy $[10^{-6}, 10^{-1}]$ kton TNT at the Earth). In particular, the more energetic impacts saturate the detectors of the two channels frequently. On the other hand, results suggest that the less energetic impacts are properly detected. Notably, more than the 99% of the detected impacts are resolved without saturating the detectors. That because of how meteoroids are distributed with respect to their impact kinetic energy.

Next, an investigation about how the dichroic wavelength affects the SNR has been performed. Results are shown in Fig. 8. The SNR curves have been plotted against the impact kinetic energy in Earth equivalent and for different values of the dichroic wavelength, in particular from 800 nm to 900 nm, with a step of 20 nm. Only the case in which half of the flash signal is contained in the pixel and LUMIO is at the average distance from the centre of the Moon is shown.

As expected, considering the VIS channel and given an impact kinetic energy, the higher the dichroic wavelength, the higher the SNR. Moreover, the higher the dichroic wavelength and the smaller the impact kinetic energies that grant the minimum SNR and that saturate the detector. On the other hand, the opposite occurs in the NIR channel. To maximize the number of detections, the ranges of resolved flashes have to overlap as much as possible. The flexibility on the selection of the dichroic wavelength can be exploited to achieve that.

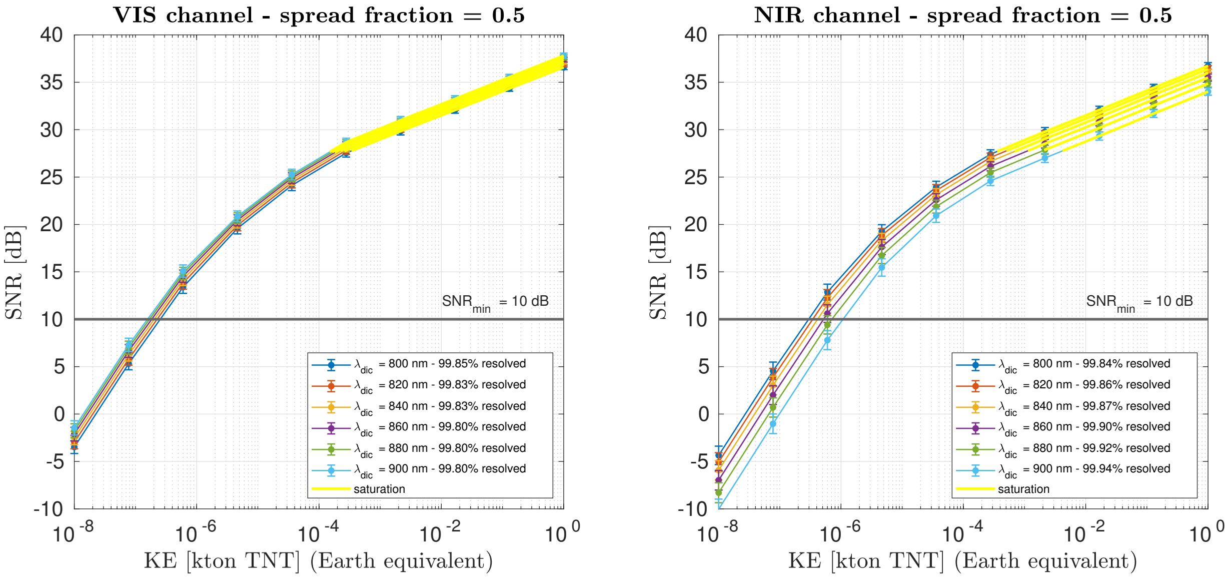

Fig. 8: Dichroic wavelength investigation. SNR as a function of the impact kinetic energy in Earth equivalent. SNR trends in the two channels for different dichroic wavelengths. In yellow, impact kinetic energies that saturate the detectors. The black horizontal line marks the threshold of minimum SNR. Legends contain the percentage of resolved impacts. Gain fixed to 10. Case of spread fraction equal to 1/2. CubeSat at distance $r_{\text{mean}} = 61\,048\,\text{km}$ from the Moon. For each given impact kinetic energy, 1000 impacts have been simulated. Stray light noise neglected. Semi-log scale plots.

Fig. 9 shows the investigation about the detectability range of impact kinetic energies. The results are shown both for VIS and NIR. The first set of curves, marked with full circles, shows how the distance at which the minimum SNR is achieved varies with respect to the impact kinetic energy in Earth equivalent given a value of the camera gain. On the other hand, the second set of curves, marked with full triangles, shows the distances at which the detectors saturate as a function of the impact kinetic energy and fixing the camera gain. To draw the curves, only the case in which half of the flash is contained in the pixel, corresponding to a value of the spread fraction equal to 1/2, has been considered.

The charts in Fig. 9 can be used to select the proper gains for the channels depending on the distance of LUMIO from the Moon. Indeed, given a distance and a gain, the set of impact kinetic energies between the two curves represents the detectability range at that distance and for that specific gain. Given a distance, the idea is to select the gain that maximizes the detectability range. From a different perspective, one can select the gain to customize the detectability range at a certain distance in order to satisfy specific requirements of the mission.

Note that the curves describing the saturation condition when the gain is 1 and 10 are very close. That is because two different kinds of saturation occur in the detectors. In the first case is the pixel that saturates. Differently, the second happens when the multiplication register saturates. In the case of $G = 1$, the pixel reaches its maximum capacity before the multiplication register possibly causing *bleeding* effect, which is definitely undesired. On the other hand, when G is greater than or equal to 10, the multiplication register reaches its maximum capacity first. The results suggest that selecting the gain $G = 10$ avoids the insurgence of the *bleeding* effect and increases the detectability range. Specifically, at greater distances, the more energetic impacts are resolved without losing performance at lower impact kinetic energies.

Finally, the selected values of the gains of VIS and NIR channels are presented in Fig. 10. The chart shows the selected gains at different distances of LUMIO from the centre of the Moon. The values of the gains have been selected to maximise the observed range of impact kinetic energy accordingly with the LUMIO mission goals and with the results presented in Fig. 9.

6 Payload data return estimation

An estimation of the scientific data budget of the LUMIO mission has been performed to infer the data requirements. The estimation of the scientific data budget has been assessed exploiting MeGun and assuming the following scientific products to be downloaded:

- picture tiles of 50 × 50 pixels (frames cropped

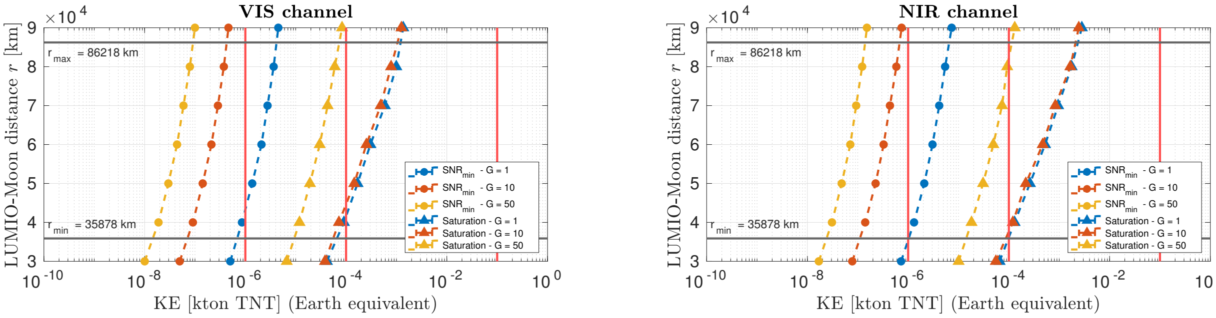

Fig. 9: Detected range of impact kinetic energies. The first set of curves, marked by full circles, shows the distance at which the minimum SNR (10 dB) is achieved as a function of the impact kinetic energy in Earth equivalent. The second set of curves, marked by full triangles, shows the minimum distance at which the detector saturates as a function of the impact kinetic energy in Earth equivalent. Plots drawn for both channels and for different LUMIO-Cam gains. The red vertical lines mark the two ranges of impact kinetic energies of interest for the mission. The black horizontal lines mark minimum and maximum distances of LUMIO during the operative phase. Case of spread fraction equal to 1/2. Given distance and gain, the set of impact kinetic energies between the two curves is the detectability range. The gain can be properly selected to maximize the detectability range at every distance. Stray light noise neglected. Semi-log scale plots.

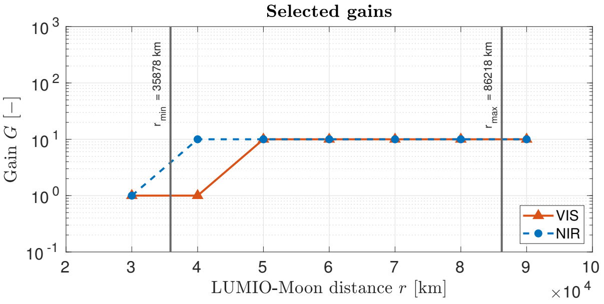

Fig. 10: Selected gains of both VIS, red triangles, and NIR, blue circles, as a function of the LUMIO–Moon distance. The black horizontal lines mark minimum and maximum distances of LUMIO in the operative phase. Semi-log scale plot.

around the flash);

- 5 tiles saved per impact;
- 2 channels working synchronously (tiles from both channels downloaded);
- 2 bytes (16 bits) per pixel.

Moreover, since not all the meteoroids generated by MeGun can be observed by LUMIO, only the potentially detected impacts are retained. The events not retained are those already specified in Section 4.1.

The Monte Carlo analysis carried out is completely focused on the year 2024. The results are shown in Fig. 11. The statistical results have been obtained running 1000 scenarios. From the plot it is very clear when LUMIO cannot perform the observation due to the unfavourable illumination conditions of the Moon. Indeed, there are periods approximately long 15 days that repeat periodically in which no scientific data are produced. These periods shift in time from year to year. Note that during the year 2024, the daily data rate in correspondence of the Geminids shower is particularly high, reaching a peak greater than 1000 Mbit/deg. That because, in year 2024, the favourable illumination condition allows to observe the peak of the Geminids meteoroid shower. For what concerns the overall scientific data budget, approximately 25 Gbit of data are expected to be produced for an operative phase lasting 1 year.

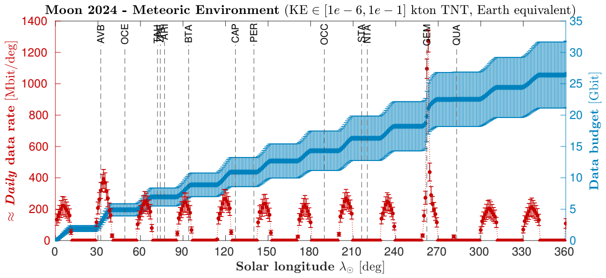

Fig. 11: Payload data return estimation – year 2024. On the y-left axis, in red, daily data rate as a function of solar longitude. On the y-right axis, in blue, cumulated data budget as a function of solar longitude. 1 year time window, from 01/01/2024 to 01/01/2025. Results shown in 1 deg bins. Stray light noise neglected. Statistical results obtained from 1000 runs.

7 Conclusions

In this paper, a prediction of the outcome of the LUMIO CubeSat has been presented. The LUMIO-POE tool used to estimate the scientific return of the mission has been introduced. An overview of the meteoroid model used in the numerical simulation and of MeGun has been provided. MeGun embeds a catalogue of meteoroid showers and sporadic sources built using experimental data taken from literature. The modelling of the LUMIO-Cam has been discussed too. Assuming that the operative phase will occur in 2024, estimations of the scientific output and of the impact dynamics have been presented, together with the results coming from the performed radiometric analysis. Finally, an estimation of the payload data return has been discussed.

Based on the results of the scientific output estimation, the mission shall observe up to 133 impacts per day (due to the Geminids peak which is expected to be observed assuming the operative phase will occur in 2024) in the range $[10^{-6}, 10^{-1}]$ kton TNT (equivalent kinetic energy at the Earth) during meteoroid showers. Additionally, LUMIO shall observe up to 31 impacts per day due to sporadic events in the same kinetic energy range. Furthermore, estimation of the equivalent black body temperature of the flash, the duration of the flash, and the size of the plume area have been computed and collected in Tab. 3. Note that the stray light noise has been neglect in this preliminary analysis. It is expected that the number of estimated detections will decrease when the stray light noise will be taken into account.

The investigation on the dichroic wavelength suggests that a slightly larger wavelength should be chosen to enhance the number of detections. In order to maximize the kinetic energy range detected by the LUMIO-Cam and mitigate the bleeding effect occurrence, proper values of the gain have been selected for both channels as a function of the LUMIO-Moon distance. According to the radiometric analysis results, the design of the LUMIO-Cam satisfies the payload functional requirements of the LUMIO mission.

From the estimated payload data return, a peak in the daily rate of scientific data produced is expected during the Geminids meteoroid shower. Overall, approximately 25 Gbit of scientific data are expected to be generated during the operative phase of the mission.

The LUMIO-POE methodology and the results presented in this work have been used to infer the science and data requirements of the mission and to verify the satisfaction of the payload functional requirements. In a future work, stray light noise will be modelled and included in the estimation of the scientific output and in the radiometric analysis. Moreover, an integrated analysis with LUMIO-POE will be performed.

Acknowledgments

Part of this work has been conducted under ESA Contract No. 4000130257/20/NL/AS under the General Support Technology Programme (GSTP) and has received support from the national delegations of Italy (ASI), the Netherlands (NSO) and Norway (NOSA). The authors would like to acknowledge the members of the LUMIO team for their contributions and the ESA CDF team in reviewing and iterating the Phase 0 LUMIO design.

Bibliography

[1] Z Ceplecha, J Borovička, W G Elford, D O ReVelle, R L Hawkes, V Porubčan, and M Šimek. Meteor phenomena and bodies. *Space Science Reviews*, 84(3-4):327–471, 1998. DOI: 10.1023/A:1005069928850.

[2] J Oberst, A Christou, R Suggs, D Moser, I J Daubar, A S McEwen, M Burchell, T Kawamura, H Hiesinger, K Wünnemann, et al. The present-day flux of large meteoroids on the lunar surface—a synthesis of models and observational techniques. *Planetary and Space Science*, 74(1):179–193, 2012. DOI: 10.1016/j.pss.2012.10.005.

[3] L R Bellot Rubio, J L Ortiz, and P V Sada. Luminous efficiency in hypervelocity impacts from the 1999 lunar leonids. *The Astrophysical Journal Letters*, 542(1):L65–L68, 2000. DOI: 10.1086/312914.

[4] Detlef Koschny and Jonathan McAuliffe. Estimating the number of impact flashes visible on the Moon from an orbiting camera. *Meteoritics and Planetary Science*, 44(12):1871–1875, 2009. DOI: 10.1111/j.1945-5100.2009.tb01996.x.

[5] J M Madiedo, J L Ortiz, F Organero, L Ana-Hernández, F Fonseca, N Morales, and J Cabrera-Caño. Analysis of moon impact flashes detected during the 2012 and 2013 perseids. *Astronomy & Astrophysics*, 577:A118, 2015. DOI: 10.1051/0004-6361/201525656.

[6] D W Hughes. P/halley dust characteristics-a comparison between orionid and eta aquarid meteor observations and those from the flyby spacecraft. *Astronomy and Astrophysics*, 187:879–888, 1987. DOI: 10.1007/978-3-642-82971-0_149.

[7] T J Jopek and Z Kaňuchová. Iau meteor data center—the shower database: a status report. *Plan-*

etary and Space Science, 143:3–6, 2017. DOI: 10.1016/j.pss.2016.11.003.

[8] D E Moser, B F Hardin, and D Janches. Meteoroids: The smallest solar system bodies. 2011.

[9] P Jenniskens, T J Jopek, J Rendtel, V Porubcan, P Spurny, J Baggaley, S Abe, and R Hawkes. On how to report new meteor showers. *Ongoing meteor work*, page 19, 2009.

[10] P Jenniskens. Meteor stream activity i. the annual streams. *Astronomy and Astrophysics*, 287:990–1013, 1994.

[11] D W R McKinley. *Meteor science and engineering.* New York, McGraw-Hill, 1961.

[12] P Jenniskens and P M M Jenniskens. *Meteor showers and their parent comets.* Cambridge University Press, 2006.

[13] P B Babadzhanov and G I Kokhirova. Densities and porosities of meteoroids. *Astronomy & Astrophysics*, 495(1):353–358, 2009. DOI: 10.1051/0004-6361:200810460.

[14] A Z Bonanos, C Avdellidou, A Liakos, E M Xilouris, A Dapergolas, D Koschny, I Bellas-Velidis, P Boumis, V Charmandaris, A Fytsilis, et al. Neliota: First temperature measurement of lunar impact flashes. *Astronomy & Astrophysics*, 612:A76, 2018. DOI: 10.1051/0004-6361/201732109.

[15] A Taylor and N McBride. A radiant-resolved meteoroid model. In *Second European Conference on Space Debris*, volume 393, page 375, 1997.

[16] J L Ortiz, J M Madiedo, N Morales, P Santos-Sanz, and F J Aceituno. Lunar impact flashes from geminids: analysis of luminous efficiencies and the flux of large meteoroids on earth. *Monthly Notices of the Royal Astronomical Society*, 454(1):344–352, 2015. DOI: 10.1093/mnras/stv1921.

[17] A Dubietis and R Arlt. Periodic variability of visual sporadic meteor rates. *Earth, Moon, and Planets*, 106(2-4):105–111, 2010. DOI: 10.1007/s11038-010-9351-6.

[18] J M Madiedo, J L Ortiz, N Morales, and J Cabrera-Caño. Midas: Software for the detection and analysis of lunar impact flashes. *Planetary and Space Science*, 111:105–115, 2015. DOI: 10.1016/j.pss.2015.03.018.

[19] P Jenniskens, Q Nénon, P S Gural, J Albers, B Haberman, B Johnson, R Morales, B J Grigsby, D Samuels, and C Johannink. Cams newly detected meteor showers and the sporadic background. *Icarus*, 266:384–409, 2016. DOI: 10.1016/j.icarus.2015.11.009.

[20] C H Acton Jr. Ancillary data services of nasa's navigation and ancillary information facility. *Planetary and Space Science*, 44(1):65–70, 1996. DOI: 10.1016/0032-0633(95)00107-7.

[21] C Acton, N Bachman, B Semenov, and E Wright. A look towards the future in the handling of space science mission geometry. *Planetary and Space Science*, 150:9–12, 2018. DOI: 10.1016/j.pss.2017.02.013.

[22] G Merisio. *Payload, Orbit, and Environment Simulation for LUMIO Mission Coverage Analysis (MSc Thesis).* Politecnico di Milano, Milan, Italy, 2019.

[23] P Brown, R J Weryk, D K Wong, and J Jones. A meteoroid stream survey using the canadian meteor orbit radar: I. methodology and radiant catalogue. *Icarus*, 195(1):317–339, 2008. DOI: 10.1016/j.icarus.2007.12.002.

[24] P Brown, D K Wong, R J Weryk, and P Wiegert. A meteoroid stream survey using the canadian meteor orbit radar: Ii: Identification of minor showers using a 3d wavelet transform. *Icarus*, 207(1):66–81, 2010. DOI: 10.1016/j.icarus.2009.11.015.

[25] P Jenniskens, Q Nénon, P S Gural, J Albers, B Haberman, B Johnson, D Holman, R Morales, B J Grigsby, D Samuels, et al. Cams confirmation of previously reported meteor showers. *Icarus*, 266:355–370, 2016. DOI: 10.1016/j.icarus.2015.08.014.

[26] P Jenniskens, Q Nénon, J Albers, PS Gural, B Haberman, D Holman, R Morales, B J Grigsby, D Samuels, and C Johannink. The established meteor showers as observed by cams. *Icarus*, 266:331–354, 2016. DOI: 10.1016/j.icarus.2015.09.013.

[27] R Walker, A Cropp, P Fernandez, M Simmonds, Q Mannes, P Concari, M Braghin, Y le Deuff, D de Wilde, A Herbertz, J van den Eynde, G Cifani, D Wegner, T Szewxzyk, J Vennekens, A Cipriano, A Piris Nino, M Branco, P Hager, L Desjonqueres, W Martens, A Kleinschneider, and L Bucci. Lumio cdf study final report, ref. cdf-r-36, february 2018, 2018.

[28] Herbert Raab. Detecting and measuring faint point sources with a CCD. In *Proceedings of Meeting on Asteroids and Comets in Europe (MACE)*, 2002.

[29] S Bouley, D Baratoux, J Vaubaillon, A Mocquet, M Le Feuvre, F Colas, Z Benkhaldoun, A Daassou, M Sabil, and Lognonné P. Power and duration of impact flashes on the moon: Implication for the cause of radiation. *Icarus*, 218(1):115–124, 2012. DOI: 10.1016/j.icarus.2011.11.028.

[30] J L Ortiz, F J Aceituno, J A Quesada, J Aceituno, M Fernández, P Santos-Sanz, J M Trigo-Rodríguez, J Llorca, F J Martín-Torres, P Montañés-Rodríguez, and E Pallé. Detection of sporadic impact flashes on the Moon: Implications for the luminous efficiency of hypervelocity impacts and derived terrestrial impact rates. *Icarus*, 184(2):319–326, 2006. DOI: 10.1016/j.icarus.2006.05.002.

[31] R M Suggs, S R Ehlert, and D E Moser. A comparison of radiometric calibration techniques for lunar impact flashes. *Planetary and Space Science*, 143:225–229, 2017. DOI: 10.1016/j.pss.2017.04.016.

[32] R M Suggs, D E Moser, W J Cooke, and R J Suggs. The flux of kilogram-sized meteoroids from lunar impact monitoring. *Icarus*, 238:23–36, 2014. DOI: 10.1016/j.icarus.2014.04.032.

[33] F Topputo, J Biggs, M Massari, K V Mani, P Di Lizia, M Nakamiya, A Cervone, R Noomen, P Sundaramoorthy, S Mestry, P Visser, E Gill, A Ivanov, M Richard, S Tulyakov, C Aas, A Jochemsen, M Sokup, J Gailis, D Labate, E Battistelli, V Reddy, and R Furfaro. Lunar meteoroid impacts observer (phase 0), 2017. Final Report, ESA SysNova Competition for Innovation No. 4, Lunar CubeSat for Exploration (LUCE), ESA ITT AO/1-8643/16/NL/GLC/as.

[34] A M Cipriano. *Orbit Design of a Lunar Meteoroid Impact Flashes Observer (MSc Thesis)*. Delft University of Technology, Delft, Netherlands, 2017.

[35] A M Cipriano, D A Dei Tos, and F Topputo. Orbit design for lumio: The lunar meteoroid impacts observer. *Frontiers in Astronomy and Space Sciences*, 5:29, 2018. DOI: 10.3389/fspas.2018.00029.